RESEARCH ARTICLE

Biofilm imaging in porous media by laboratory X-Ray tomography: Combining a non-destructive contrast agent with propagation-based phase-contrast imaging tools

Maxence Carrel[1], Mario A. Beltran[2], Verónica L. Morales[1,3], Nicolas Derlon[1,4], Eberhard Morgenroth[1,4], Rolf Kaufmann[2], Markus Holzner[1] *

1 Institute of Environmental Engineering, ETH Zürich, Stefano Franscini-Platz 5, 8093 Zurich, Switzerland, **2** Swiss Federal Laboratories for Materials Science and Technology (EMPA), Dübendorf, Switzerland, **3** Department of Civil and Environmental Engineering, University of California Davis, Davis, California, United States of America, **4** Swiss Federal Institute of Aquatic Science and Technology (EAWAG), Dübendorf, Switzerland

* holzner@ifu.baug.ethz.ch

🔓 OPEN ACCESS

Abstract

X-ray tomography is a powerful tool giving access to the morphology of biofilms, in 3D porous media, at the mesoscale. Due to the high water content of biofilms, the attenuation coefficient of biofilms and water are very close, hindering the distinction between biofilms and water without the use of contrast agents. Until now, the use of contrast agents such as barium sulfate, silver-coated micro-particles or 1-chloronaphtalene added to the liquid phase allowed imaging the biofilm 3D morphology. However, these contrast agents are not passive and potentially interact with the biofilm when injected into the sample. Here, we use a natural inorganic compound, namely iron sulfate, as a contrast agent progressively bounded in dilute or colloidal form into the EPS matrix during biofilm growth. By combining a very long source-to-detector distance on a X-ray laboratory source with a Lorentzian filter implemented prior to tomographic reconstruction, we substantially increase the contrast between the biofilm and the surrounding liquid, which allows revealing the 3D biofilm morphology. A comparison of this new method with the method proposed by Davit et al (Davit et al., 2011), which uses barium sulfate as a contrast agent to mark the liquid phase was performed. Quantitative evaluations between the methods revealed substantial differences for the volumetric fractions obtained from both methods. Namely, contrast agent—biofilm interactions (e.g. biofilm detachment) occurring during barium sulfate injection caused a reduction of the biofilm volumetric fraction of more than 50% and displacement of biofilm patches elsewhere in the column. Two key advantages of the newly proposed method are that passive addition of iron sulfate maintains the integrity of the biofilm prior to imaging, and that the biofilm itself is marked by the contrast agent, rather than the liquid phase as in other available methods. The iron sulfate method presented can be applied to understand biofilm development and bioclogging mechanisms in porous materials and the obtained biofilm

morphology could be an ideal basis for 3D numerical calculations of hydrodynamic conditions to investigate biofilm-flow coupling.

Introduction

Biofilms are ubiquitous sessile microorganisms embedded in a self-produced matrix consisting of extracellular polymeric substances (EPS) [1]. The EPS matrix protects biofilms from their environment, so that they persistently develop and survive in industrial, natural or biomedical settings [2]. In water saturated soils, most microorganisms develop sessile lifestyles [3]. Biofilms are of high interest in this context, because of their natural contribution to the bioremediation of aquifers [4] or to reactive barriers [5], to microbial enhanced oil recovery [6] or to the sequestration of carbon dioxide [7, 8]. However, the growth of biofilms in porous media and the consequent bioclogging of the pore spaces [9] can also be detrimental as it can lead to the clogging of groundwater recharge wells [10] or deep geothermal systems [11]. It can also lead to an enhanced non-Fickian spreading of solute contaminants in groundwater [12], substantially complexifying the modelling and upscaling of mass transport in these systems [13–18].

Biofilms have been described as microbial landscapes [19] stretching over a large range of spatial scales [20] ranging from the micro- (individual cells), to the meso- (biofilm patches scale) or to the macroscale (reactor, aquifer scales). Accordingly, different experimental methods have been developed to investigate processes at different scales, from optical or confocal microscopes to characterize microscale development of biofilms in flow cells [21] or microfluidic devices [22], to studies using soil columns [23, 24] and characterizing the influence of biofilms on bulk system (macro-scale) properties (permeability reduction, dispersion, degradation rates of solutes etc.).

The mesoscale, which is the scale of interest in this study, is the scale where the biofilm structure is being shaped by the interplay of the hydromechanical and mass transfer processes. In porous media, this scale approximately corresponds to the pore-scale. Many investigations for porous media at that scale were performed using optical systems [25–30], but were limited to 2 dimensions. Lately, Optical Coherence Tomography (OCT) [31–33] stood out as a very powerful method to investigate these processes at the mesoscale for many different systems. However, OCT uses low coherent light in the visible range and the opacity of 3D samples limits the penetration depth. Therefore, OCT cannot be used for 3D porous media samples. Magnetic Resonance Imaging (MRI) is a great tool to obtain both flow and biofilm stuctural information, it is limited in spatial resolution (generally resolution coarser than 50 μm) which makes it difficult to access the exact liquid and biofilm phases from the transverse relaxation times (T2) [12, 34–36].

In the last few decades, X-ray microtomography (X-ray μCT) became a standard tool for imaging soil samples [37, 38] and to image biofilm structures in 3D soil-like samples. Differentiating the biofilm from the liquid phase is a difficult task when using X-ray μCT due to the high water content of biofilms and the consequently very close X-ray attenuation coefficients of water and biofilms. As a result, it is common to use chemical agents to increase the contrast between the biofilm and liquid phases. Particulate barium sulfate ($BaSO_4$) suspensions were used as contrast agent to label non-biofilm colonized pores and imaged biofilm on a X-ray lab source [39]. Silver-coated 10 μm microspheres deposited at the biofilm surface revealed the biofilm-liquid interface using synchrotron radiation [40]. Another approach suggested was

based on the use of 1-chloronaphtalene, an immiscible liquid with water, as a contrast agent [41, 42]. Finally, numerical pore-scale biofilm growth modeling was performed based on biofilm structures obtained at different Reynolds numbers from X-ray synchrotron tomography using $BaSO_4$ as a contrast agent [43].

All the described methods based on X-ray μCT to image biofilms either used a particulate suspension or a chemical to mark the liquid phase that was introduced *a posteriori* in the biofilm containing sample. The rationales behind the approach using particulate $BaSO_4$ suspensions is first, that the $BaSO_4$ particles are micrometer-sized and behave passively. Second, that the biofilm inner channels are smaller than the micrometer-sized barium suflate particles [44] and therefore, that advection of the $BaSO_4$ particles within the biofilm is negligible. However, these rationales remind largely untested so far. Additionally, given that $BaSO_4$ is a relatively heavy compound ($\rho_{BaSO_4} = 3.62 g/cm^3$), sedimentation issues arise, which can be exacerbated by the aggregation of the particles and then lead to motion blur artifacts. The use of additives such as xantham gum stabilizes these solutions but also change the rheological properties, potentially inducing biofilm detachment [39]. On the other hand, the approach based on silver-coated microspheres [40] suffered from the heterogeneous distribution of the silver-coated microspheres and possible interactions between the dense microspheres suspensions and the biofilm were not investigated. The 1-chloronaphtalene used as a contrast enhancing agent [41, 42] also has significant drawbacks, since this liquid is immiscible with water. Therefore, the non-wetting phase curvatures and contact angles may not contour exactly the interface with the aqueous biofilm phase. Additionally, it is not guaranteed that the capillary pressure requirements to invade all unclogged pores are met. Finally, 1-chloronaphtalene is a powerful pesticide whose interactions with biofilms have not been investigated yet.

In this study, instead of adding a potentially destructive contrast agent to the liquid phase, we use iron sulfate ($FeSO_4$), a non-toxic inorganic compound naturally present in soils. $FeSO_4$ is commonly used in biofilm studies [32, 45, 46]. The rationale behind this approach is that some biofilms naturally exhibit high content of inorganic matter (e.g. mineral precipitates [47]). $FeSO_4$ is a compound naturally present in some aquifers and it can even be artificially introduced to enhance the bioremediation of contaminants (arsenic, uranium) by enhancing their precipitation [48, 49]. Here, the biofilm is cultured under the continuous addition of a solution containing $FeSO_4$ that is either bound in a dilute form within the EPS or forming colloidal matter on which the biofilm can develop. Both iron and sulfate concentrations used in this study are in the range of concentrations observed in the environment and in contaminated sites [50–52]. In order to increase the contrast and visualize the biofilm, we image the biofilm on a laboratory-based X-ray source using a relatively large source-to-detector (STD) distance. The large STD was used to exploit X-ray free space propagation in order to render visible refraction effects that take place as the X-rays travel through the sample, a technique commonly known as propagation-based phase contrast (PBI) [53, 54]. In addition, a robust Fourier filter which has the form of a Lorentzian function is applied as a digital pre-processing tool to the acquired projections to enhance the contrast and to improve the signal-to-noise ratio (SNR) [55, 56]. The presented method allows to image the 3D biofilm morphology in porous media at the mesoscale, using an X-ray lab source and a non-destructive contrast agent.

Materials and methods

Porous media and biofilm culturing

The porous media used in this study consisted of Nafion pellets (NR50 1100 EW, Ion Power, Munich, Germany) of 2.5 mm diameter similar to coarse sand grains. This material has similar physical and chemical properties to sand grains (e.g. particle size distribution or ion exchange

capacity) and its optical refractive index in the visible domain is similar to that of water [57, 58]. For the inoculation of the media, the Nafion pellets were immersed for 24 h in an aerated batch containing 500 mL of natural water sampled from a pond located on the ETH campus. After 24 h, a polymethyl methacrylate (PMMA) tubular reactor (inner diameter 10 mm, length 160 mm) was wet packed with the pellets and connected to the batch. A biofilm was cultivated for 7 days using the setup shown in Fig 1A. A 500 mL feed solution made of tap water containing 1 g/L of glucose and 100 mg/L was used and changed every 48 h. A volumetric flow rate of 5 mL/min was set which corresponds to a Darcy velocity q of 1.06 mm/s. The initial porosity (volumetric fraction of the liquid phase) ϕ is ca. 40%, which yields an average pore scale velocity $v_p \approx q/\phi$ = 2.65 mm/s and corresponding Reynolds number $Re = qd/v \approx 2.5$ and Péclet number $Pe = qd/D_{H_2O} \approx 1000$. Upon biofilm growth, the porosity decreased by a twofold factor, meaning that the average pore scale velocity doubled.

Contrast agents

A concentration of 100 mg/L of the contrast agent used in this study $FeSO_4 x7(H_2O)$ (corresponding to 56 mg/L $FeSO_4$ (20.6 mg/L Fe and 35.4 mg/L SO_4) or 0.37 mmol/L $FeSO_4$) was continuously added to the feed solution during the biofilm growth. The concentrations of both iron and sulfate compounds are in the range of concentrations observed in the environment [50–52] or used for other experimental work [32, 45, 46]. At that concentration and for the initial pH observed in this study (pH $\approx$ 7), the iron should be still soluble. However, the oxidation to Fe(III), which is less soluble and tends to form colloids, should occur quite rapidly [52]. In fact, iron flocs formed a few hours after the start-up of the system. Therefore, the inlet tubing was carefully set close to the water level, to limit the circulation of the flocs and to enhance their settling. The biofilm grown here exhibited a brownish color typical of iron oxides. Before the X-ray measurements, a volume of water corresponding to 8 times the initial pore volume was injected through the flow cell to ensure that no biofilm unbound iron was remaining in the liquid phase.

To investigate the influence of the colloidal and flocculated iron on porous medium flow and to monitor deposition of colloids inside the medium, we performed a control experiment. In that experiment, a $FeSO_4$ containing solution was recirculated through a packed tubular reactor with identical conditions as those stated above, but without inoculation.

In order to compare the results obtained from this new approach with an already existing method, we followed the approach presented by Davit et al. [39], using a particulate Micropaque® (Guerbet, Zurich) $BaSO_4$ suspension as a contrast agent that was introduced into the liquid phase after the growth of the biofilm. $BaSO_4$ suspensions are used to image biofilms in porous media because of the high attenuation coefficient of barium. Another advantage is that the $BaSO_4$ particles are micrometer-sized and should therefore be physically size excluded from the EPS matrix [44]. Micropaque® suspensions have a particle size distribution close to 1 μm (according to the manufacturer of the product, 25% $\leq$ particles larger than 2 μm, 20% $\leq 0.5\mu m$ an average diameter of 1.25 μm). These suspensions also contain additional stabilizing agents (e.g. xanthan gum, polydimethylsiloxane (PDMS) or sodium citrate etc.) that prevent the aggregation and sedimentation of the particles but strongly influence the rheological properties of the suspension. Plouraboué et al. [59] showed that the Micropaque® barium suflate suspensions exhibited a viscosity much higher than water and a shear-thinning behavior similar to that of blood (see Fig 1.b in Plouraboué et al. [59]). Here, a Micropaque® suspension of 0.1 g/L $BaSO_4$ concentration was injected in the tubular reactor at 10% of the volumetric flow rate applied during the biofilm culturing in an attempt to avoid forced detachment due to the injection of the contrast agent. Due to dispersion and dilution effects, the
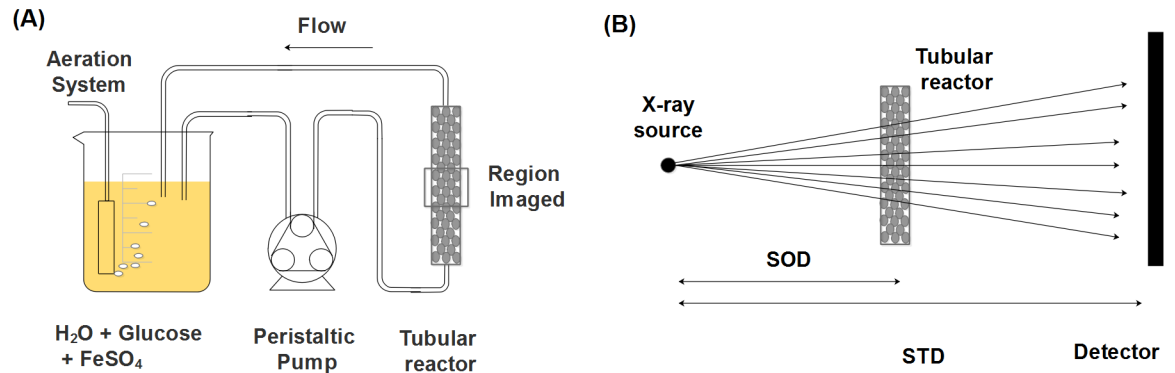
Fig 1. (A) Schematic of the experimental setup used for the biofilm culturing as well as the region of the tubular reactor used for biofilm imaging. (B) Schematic of the configuration used for the X-ray scans where the distances SOD and STD represent the source-to-object (SOD) and the source-to-detector distance (STD).

https://doi.org/10.1371/journal.pone.0180374.g001

distribution of the $BaSO_4$ in the reactor was inhomogeneous after 1 pore volume. Therefore, 2 times the initial pore volume of the tubular were injected to completely saturate the tubular reactor with the suspension. Although the injection was done carefully and at a flow rate 10 times smaller than the one used for water, significant biofilm detachment was visually observed during the injection.

X-ray imaging

Table 1 provides an overview of the different imaging conditions and image analysis approaches for the four datasets obtained from three different scans performed in the frame of this work. A first scan was performed with the sample containing the biofilm stained with $FeSO_4$ only. For this scan (used to obtain the $FeSO_4$ and $LFeSO_4$ datasets), the source-to-object

Table 1. Information relative to the different scans and datasets used in this work as well as the corresponding details concerning the data analysis.

Dataset	$FeSO_4$	$LFeSO_4$	$BaSO_4$	$LControl$
Tubular reactor Nr	1	1	1	2
Scan Nr	1	1	2	3
Biofilm Growth	Yes	Yes	Yes	No
Contrast agents	$FeSO_4$	$FeSO_4$	$FeSO_4 \& BaSO_4$	$FeSO_4$
Source to detector distance (mm)	2330	2330	1017	2330
Scan details	50 kV, 190 μA	50 kV, 190 μA	80 kV, 190 μA	50 kV, 190 μA
Scan resolution (μm)	9	9	21	9
Projection image processing prior to reconstruction	-	Lorentzian filter	-	Lorentzian filter
Image filtering prior to segmentation	-	3D curvature-driven diffusive filter	3D curvature-driven diffusive filter	3D curvature-driven diffusive filter
Segmentation approach	-	VG Max surface determination	Seeded region growing algorithm & VG Max surface determination	VG Max surface determination
Registered dataset	No	Yes	Yes	No

https://doi.org/10.1371/journal.pone.0180374.t001

distance (SOD) was of 130 mm and the source-to-detector distance (STD) was set to the largest possible distance, 2330 mm (see Fig 1B). As mentioned previously, this fairly large STD distance was chosen to enhance the refraction effects occuring as the X-rays travel through the sample. The custom made tomographic setup was equipped with a microfocus X-ray tube (Viscom XT9160-TDX) and a 40 x 40 cm^2 flat panel detector (Perkin Elmer XRD 1621) with 200 x 200 μm^2 pixels. Since biofilms weakly absorb X-rays, the source had to be operated at a voltage of 50 kV and and a focused electron beam current (FEC) of 190 μA. 1441 projections with a field of view (FOV) of 1.85 x 1.85 cm^2 were gathered at 0.25˚ angle steps with two frames per projection at a resolution of 9 μm. For the second scan ($BaSO_4$ dataset), the same sample was used (see Table 1). The SOD distance was unchanged and the STD distance was reduced to 1017 mm, which would correspond to a reasonable distance for standard X-ray attenuation-based imaging. The voltage was set to 80 kV and the FEC to 120 μA. 1441 projections with a FOV of 4.3 x 4.3 cm^2 were gathered at 0.25˚ angle steps with three frames per projection at a resolution of 21 μm. The difference in resolution between both scans is due to the fact that the SOD stayed constant and the STD decreased, reducing the physical magnification. For the last scan (control dataset LControl), the settings were the same as for the first one. Due to the rather low contrast of the projections and variations in the source intensity the projections were normalised to reach a reasonable contrast in the 3D volume. This pre-processing and the reconstruction were performed on in-house developed software tools based on filtered back-projection [60]. The scanning times were of ca. 3 hours.

Image analysis

Image preprocessing by means of a Lorentzian filter. A key step for the results produced with the $FeSO_4$ data is the application of an image processing Lorentzian filter in Fourier space to each radiographic projection before tomographic reconstruction. To evaluate the utility of the Lorenztian filter, the data from the first scan was reconstructed with and without applying this filter ($LFeSO_4$ resp. $FeSO_4$ datasets) and also applied to the control dataset (LControl, see Table 1). The filter presented here substantially reduces noise and enhances contrast. It is based on the original work of [61] where it was initially developed as a method to retrieve phase-and-amplitude information from inline propagation-based X-ray holograms using monochromatic beams and specifically for single-material samples. Here, the monochromaticity and single material assumptions are discarded and the algorithm is used *strictly* as an image processing tool, which exploits its high numerical stability under the presence of noise. This stability was shown in previous studies to greatly improve the contrast and the signal quality both in simple projection imaging as well as tomography [55, 56, 62–66]. The Lorentzian filter used here has the following form:

$$I^{Filt} = F^{-1}\left[\frac{1}{\alpha \mathbf{k}_{\perp}^2 + 1} F\{I^{Rad}\}\right] \tag{1}$$

Here, I^{Rad} is the acquired radiographic image at a particular orientation. I^{Filt} is the filtered image once the Lorentzian filter is applied to I^{Rad}. The symbols F and F^{-1} are the forward and inverse Fourier transforms. $\mathbf{k}_{\perp} = (k_x, k_y)$ are the transverse Fourier space coordinates reciprocal to the real space coordinates $\mathbf{r}_{\perp} = (x, y)$. In other words, the operation in Eq (1) is as follows: (i) Take the Fourier transform of the image I^{Rad}, which in this case serves as input data; (ii) multiply the result by the Fourier space Lorentzian function $\frac{1}{\alpha \mathbf{k}_{\perp}^2 + 1}$ and; (iii) take the inverse Fourier transform thus attaining the filtered image I^{Filt}; (iv) perform the tomographic reconstruction using the backprojection method mentioned earlier. The filter was implemented as a Matlab® routine [67]. The non-negative real valued constant α is an important parameter of
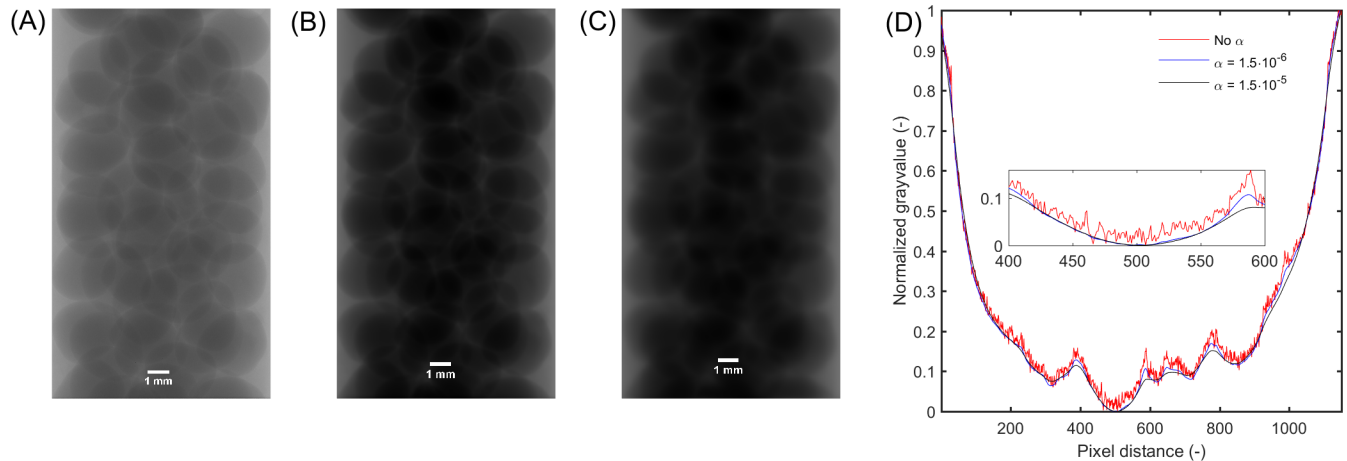
Fig 2. (A) raw projection image (unfiltered). (B) Lorentz filtered image of (A) using $\alpha = 1.5 \cdot 10^{-7}$. (C) Lorentz filtered image of A using $\alpha = 1.5 \cdot 10^{-8}$. The same dynamic range was used for (A), (B) and (C) for the sake of comparison. (D) displays horizontal normalized profiles at the location of the dashed line in (A), and (B) and (C) as well as for additional values of α. The inset shows a magnification of the gray value profile at the center of the tubular reactor. The scale bar in (A) is also valid on (B) and (C).

the filter. It is important to mention that in the original form of the algorithm (see [61]), the value of α was known *a priori* since it is meant specifically to deal with only single material specimens. However, for our purposes, we use it as a *tuning parameter* that may be adjusted according to how much noise one desires to remove without over-blurring key features (edges) in the reconstructions. To obtain a good estimate of α we use a strategy that takes a raw projection image from the CT set which is used as reference and then graphically compared to a filtered image. An example of this strategy is seen in Fig 2. Here, we have an unfiltered radiographic image I^{Rad} in Fig 2A and a Lorentz filtered I^{Filt} version of the same image in Fig 2B and 2C obtained with values of α of $1.5 \cdot 10^{-6}$ and with $1.5 \cdot 10^{-5}$, respectively. In this work, an α value of $1.5 \cdot 10^{-6}$ was used. In Fig 2D, gray value profiles of images (A), (B) and (C) across the same horizontal line are shown enabling a graphical comparison. These profiles show how the blue curve corresponding to (B) displays significantly less noise than the red curve corresponding to (A). In addition to noise reduction we see that the blue profile corresponding to (B) also follows the same trend than the red one. This is illustrated more clearly in the inset showing a magnified region of the profiles. For the other value of α ($\alpha = 1.5 \cdot 10^{-5}$), both (C) and (D) (black), the effect of the over-blurring is evident. The balance of noise reduction and trend matching provides us a qualitative, yet clear visual indication whether our value chose for α is neither over- nor underestimated.

The effectiveness of the Lorentzian filter from a tomographic perspective is illustrated in Fig 3. Here, we show tomographic slices of the same region with (A) and without (C) applying the Lorentzian filter before reconstructing. From this example it is evident that applying the Lorentzian filter prior to reconstruction greatly improves the visualization of the biofilm/water interface in the tomographic reconstruction. Fig 3B and 3D show gray value profiles labeled P1 and P2 clearly illustrating a reduction of noise. Boundaries still remain well defined after the application of the Lorentzian filter.

Segmentation. Since two different contrast agents were used, it was not possible to define one segmentation procedure and apply it to all datasets so that a single approach was defined for each contrast agent. After reconstruction of the $LFeSO_4$ dataset, the image contrast was
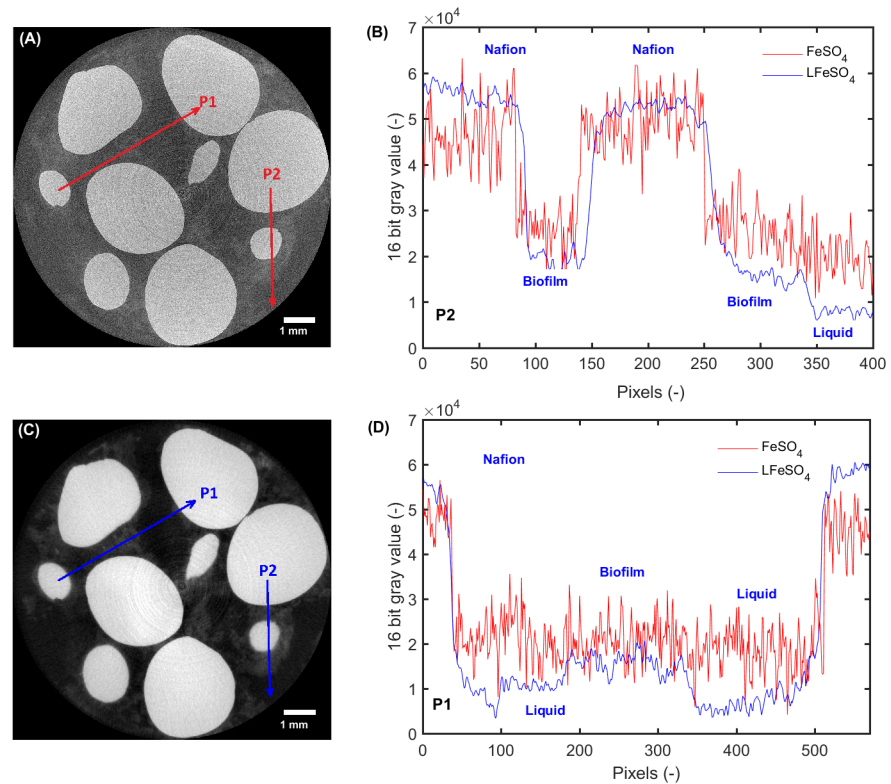
Fig 3. Slices from the FeSO₄ (A) and LFeSO₄ (C) datasets. For the sake of comparison, both images were normalized with 0.4% of the pixels saturated. The two red resp. blue arrows indicate the location and direction at which the gray value profiles are extracted. The scale bar represents 1 mm. Gray value profile for the first (P1, (D) and the second location P2, (B)). The profiles are labeled with the different phases observed.

enhanced so that the Nafion grains were mostly saturated. A curvature-driven diffusion filter was then run in Avizo® (5 iterations and standard parameters: sharpness = 0.9, anisotropy = 0.6), reducing the noise while preserving the edges. Fig 4A shows a slice (located at the middle of the stack) obtained after the filtering and Fig 4C (red) shows the 8 bit gray value histogram obtained for the whole stack. On that histogram, the peaks corresponding to the liquid and Nafion phases are clearly identifiable. The liquid phase peak exhibits a strong shoulder on its right side, that corresponds to the biofilm phase. The overlap between the liquid and biofilm regions as well as the strong tail exhibited by the biofilm shoulder are due to the heterogeneous gray value distribution of the biofilm region (see Fig 4A). In order to segment these two regions, we assumed two overlapping peaks for the biofilm and the liquid phase and fixed a threshold at the inflection point located between the liquid phase peak and the biofilm shoulder. The determination of this inflection point is related to some uncertainty (see Supplementary Information). We therefore performed a simple sensitivity analysis by defining three different thresholds at the center and lower resp. higher end of the shoulder region. These thresholds are illustrated in purple, resp. yellow and green in Fig 4C). The gray values used for the sensitivity analysis correspond to ca. 10% of the central gray value (purple). For all threshold values, a thresholding was performed in VG Max®. Then, a closing operation was done in order to fill in small voids that are considered as noise from each phase. A region growing algorithm was used to identify disconnected segments of biofilm or liquid (e.g. pores in the biofilm
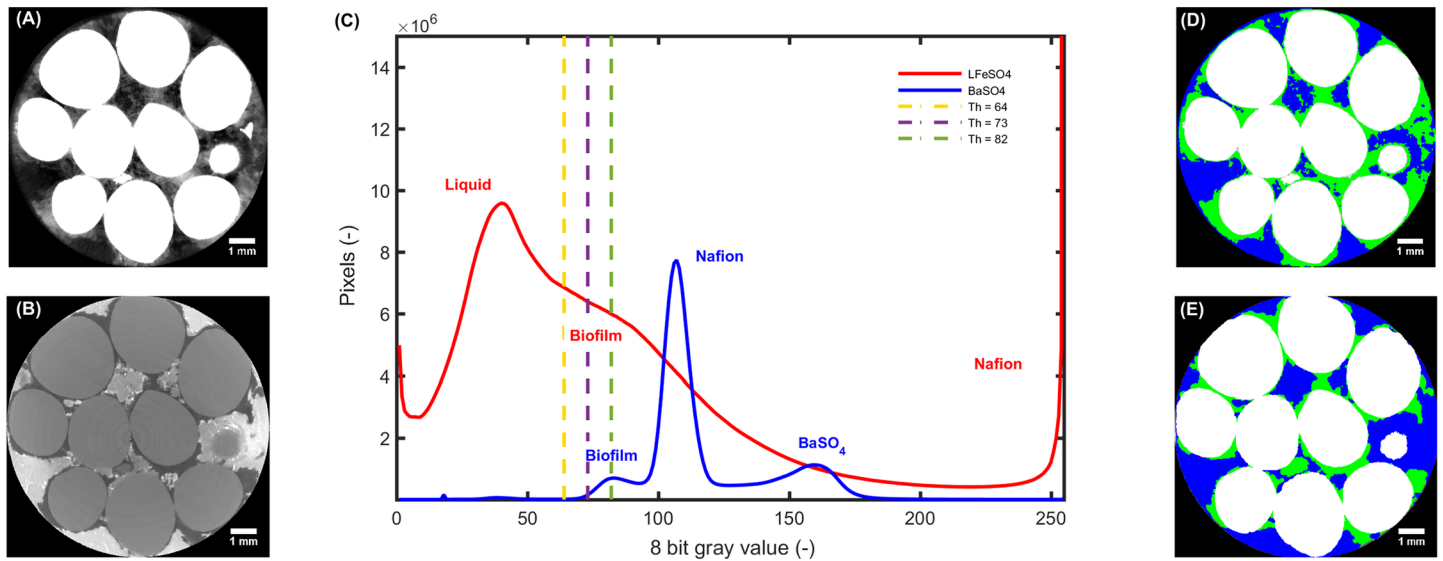
Fig 4. Middle slices (filtered prior to segmentation according information in Table 1) for the *LFeSO₄* (A) and *BaSO₄* (B) datasets. The corresponding 8 bit gray value histograms are shown in C) for the *BaSO₄* (blue) dataset and for the *LFeSO₄* (red) dataset after contrast enhancement and application of the 3D curvature-driven diffusive filter. For the *LFeSO₄* dataset, the vertical dashed lines in yellow, purple and green correspond to isosurface values of 64, 73 and 82 used for the segmentation and the corresponding sensitivity analysis. The peaks corresponding to the different phases are annotated. (D) and (E) show the segmented datasets where the solid, liquid and biofilm phases are color coded in white, blue and green respectively. The scale bar represents 1 mm.

or floating biofilm bits) that were merged into the surrounding phase. Since we observed the formation and displacement of air bubbles during the flushing out of the remaining iron or the injection of $BaSO_4$, the air bubbles were segmented and merged into the liquid phase. The result of this segmentation is shown in Fig 4D).

Fig 4B shows a slice (same location than for Fig 4A, in the middle of the stack) of the $BaSO_4$ dataset obtained after application of the same 3D curvature driven filter. The corresponding histogram of the $BaSO_4$ dataset (see Fig 4C, in blue) shows a peak for the Nafion grains (central peak) and two additional peaks for the biofilm and the liquid phase. As it it shown in Fig 4B, due to the high attenuation of $BaSO_4$, this dataset exhibited some beam hardening artifacts. These artifacts were overcome in the segmentation by using the ImageJ implementation [68, 69] of a seeded region growing algorithm [70] providing satisfying segmentation of the solid phase (see Supplementary Information for details). The liquid and biofilm phases were then obtained by thresholding after using the segmented solid phase as a mask. Fig 4E shows the corresponding segmented result. A sensitivity analysis was performed for that thresholding and is presented in the Supplementary Information. Finally, the control sample was imaged and segmented following the same approach as for the $LFeSO_4$ dataset.

Registration of the two different datasets. A registration (volumetric image alignment onto a single coordinate system) of the two different tomograms was performed in order to compare locally (e.g. conditional probabilities) the volumetric fractions obtained from the different datasets. To begin with, the resolution of both datasets was matched. Then, a coordinate alignment process was performed in Matlab® on the solid phases, because these are the most similar phases in both datasets. Here, the *imregister* function with default parameters was used for finding and optimizing an affine geometric transformation minimizing a mean square error metric. The optimization of the registration was performed using a regular step gradient
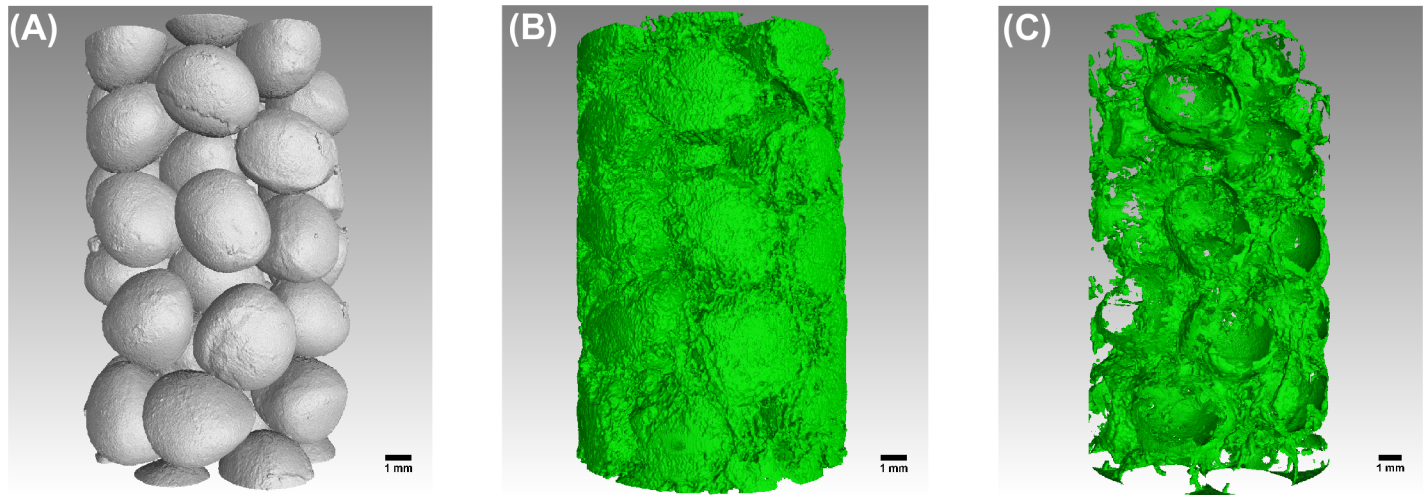
Fig 5. Three-dimensional renderings of the solid phase (left), of the sample imaged with FeSO₄ (center) and barium suflate (right) as a contrast-enhancing agents.

descent method. All the results and analyses presented in the following were obtained from the registered datasets.

Results

Fig 4(A) and 4(B) show slices of the LFeSO₄ and BaSO₄ datasets obtained after filtering with a 3D curvature-driven filter. On both images, the biofilm is visible (light gray zones in) A) and the darkest ones in (B) but it seems that there is substantially more biofilm on image (A). The biofilm gray values in (A) exhibit an important heterogeneity. On this image, it is possible to identify darker zones belonging to the liquid phase and lighter ones to the biofilm. Fig 4(D) and 4(E) show the corresponding segmented slices where the segmented biofilm phases obtained with both contrast agents roughly overlap. However, on both the pre-processed (Lorentzian when used and 3D curvature-driven filtering) and segmented images, some biofilm regions locally do not match. Fig 5. shows 3D renderings of the solid phase (Nafion grains) and the segmented datasets which reveal that the volume fraction of the biofilm (green) is much smaller for the BaSO₄ dataset. Qualitatively, the biofilm appears more patchy for the BaSO₄ than for the LFeSO₄ dataset. For the latter, the biofilm exhibits complex corrugated shapes that are more interconnected. It appears that greater detail of the biofilm morphology is resolved when LFeSO₄ is used as a contrast enhancing agent.

Fig 6. shows volumetric fraction profiles along the streamwise direction for the LFeSO₄ and for the BaSO₄ datasets. The average total volumetric fractions obtained are given in the legend. The profiles obtained for the solid phase of both samples show a very good overlap and have volumetric fractions that are relatively close, at about 60% of the whole volume of the sample. The oscillations of these values present a wave length of ca. 2.5 mm approximately corresponding to the grain size diameter, indicating that there is some degree of order in the packing. While there is a good matching for the volumetric fractions profiles obtained for both solid phases, it is not the case for the remaining phases. For instance, the biofilm fraction obtained for the LFeSO₄ dataset is about three times larger than for the BaSO₄ dataset. The shaded region is delimited by the lower and higher thresholds used for the sensitivity analysis. Over
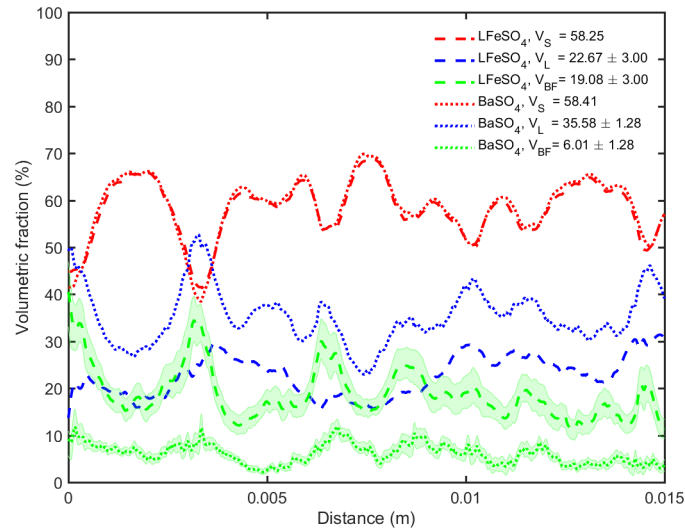
Fig 6. Profiles of the volumetric fractions (S: solid, L: liquid, BF: biofilm) obtained for the different datasets (BaSO$_4$: small dashes, FeSO$_4$: longer dashes). The shaded region is defined by the results obtained for the threshold sensitivity analysis. For the sake of clarity, the results of this sensitivity analysis are not added to the liquid phases. The average volumetric fractions (in percent) for the different phases (Solid V_S, Liquid V_L, Biofilm V_{BF}) obtained with the two different contrast-enhancing agents is given in the legend.

the whole column, the biofilm volumetric fraction obtained with FeSO$_4$ is consistently larger than for the BaSO$_4$ dataset (about twice as much).

To study how the phases overlap in 3D space, we locally computed the conditional probabilities of the phase overlap between the two different datasets, e.g. the percentage of a first phase corresponding to the same phase in a second one ($P(A \mid B) = P(B \cap A)/P(B)$) (see Table 2). With more than 90% in both cases, the overlap is very good for the solid phases. Again, the remaining phases exhibit substantial differences. For the biofilm phase, the intersection of voxels identified as biofilm in both BaSO$_4$ and LFeSO$_4$ datasets only correspond to ca. 25% against ca. 70% for the opposite case. This indicates two different aspects: first that locally the volumetric fraction of the biofilm obtained for the LFeSO$_4$ dataset is substantially higher than for the BaSO$_4$ dataset. Secondly, as biofilm patches detached upon the BaSO$_4$ injection, they might have reattached or filtered at some other locations within the column where there is no biofilm visible in the LFeSO$_4$ dataset.

The control sample was treated in the same way than the FeSO$_4$ data set, except for the fact that it was not inoculated with the bacterial inoculum and that no growth medium was added for the 7 days. The image processing (filters, reconstruction and segmentation) used was also the same as the one used for the FeSO$_4$ data set. The aim of this control was to estimate the concentration of colloidal FeSO$_4$ in the biofilm itself. For the control, a colloidal volumetric fraction of about 10% was obtained, indicating that the iron equalled ca. 54% of the volumetric fraction of the biofilm. This indicates that the inorganic content of the biofilm cultivated here is fairly high.

Discussion

In this study, the combination of a non-destructive contrast agent, a long STD and Lorentzian filtering revealed intact 3D biofilm morphologies in porous media. This particular

Table 2. Conditioned probabilities that a given phase in the FeSO4 data locally belongs to the same phase in the BaSO4 data computed for the solid (S), liquid (L) and biofilm (BF) phases for the registered Lorentz filtered FeSO$_4$ and BaSO$_4$ datasets.

| Conditional probability	Percentage
$P(S_{BaSO_4} \mid S_{LFeSO_4})$	93.85
$P(S_{LFeSO_4} \mid S_{BaSO_4})$	98.18
$P(L_{BaSO_4} \mid L_{LFeSO_4})$	88.20
$P(L_{LFeSO_4} \mid L_{BaSO_4})$	54.25
$P(BF_{BaSO_4} \mid BF_{LFeSO_4})$	24.74
$P(BF_{LFeSO_4} \mid BF_{BaSO_4})$	72.57

combination of contrast agent and imaging tools borrowed from phase contrast imaging allowed to substantially reduce noise and improve the contrast of the sample containing materials with small attenuation coefficient differences.

The different volumetric fraction obtained for the BaSO$_4$ and FeSO$_4$ contrast agents could be explained by the following reasons: uncertainty related to the segmentation or the registration, partial volume effects due to the different imaging resolution and interactions between the BaSO$_4$ suspension and the biofilm (e.g. penetration or invasion of the biofilm and biofilm detachment upon the introduction of the contrast agent). The volumetric fraction obtained for the biofilm is sensitive to the threshold considered, but in all cases stays consistently higher than the BaSO$_4$ volumetric fraction. The good agreement of both the average volumetric fractions and volumetric fractions profiles of the solid phase illustrated in Fig 6. allows us to rule out the uncertainty related to the registration or the partial volume effects as a main cause for the mentioned substantial differences. Therefore, penetration of the smallest BaSO$_4$ particles within the biofilm and biofilm detachment (as illustrated schematically in Fig 7.) appear to be at the root of the differences observed.

About 20% of the BaSO$_4$ particles used have a diameter smaller than 0.5 *μm* and are smaller than the largest biofilm pores expected [44]. In the present case, it is realistic to assume that a portion of the smallest BaSO$_4$ particles could enter the biofilm channels (see Fig 7.) and therefore labelling the parts of the biofilm as liquid.

As mentioned earlier, biofilm detachment was observed during the injection of BaSO$_4$ (see Supplementary Information). This observation was already noted previously in another study [39]. We estimated the average wall shear stress exerted by the BaSO$_4$ suspension on the biofilm assuming a power law fluid flowing in a simplistic representation of an average pore in our system. Although the flow rate was 10 times smaller during the BaSO$_4$ injection than the growth flow rate, we found ca. 3 times higher wall shear stresses in the BaSO4 injection stage due to the high viscosity and shear thinning properties of the BaSO4 suspension. Given the extremely wide range of shear rates taking place in the actual porous medium [58], locally the wall shear stresses ratio might be significantly higher, causing the detachment observed. In such a case, the rheological properties of the BaSO$_4$ suspension should not be neglected.

Derlon et al. [71] and Rochex et al. [72] showed that biofilm form stratified structures and that the biofilm resistance to shear or shear strength [73] is dependent on the wall-normal location within the biofilm. Möhle et al. [46] showed that by increasing the biofilm shear strength, high concentrations of iron in biofilms had a positive effect on the biofilm stability. Here, lower shear strength regions of the biofilm probably detached upon BaSO$_4$ injection and the basal layers with higher shear strength remain attached. Abrasion of biofilm by particles is another known detachment mechanism [71]. It is not excluded that BaSO$_4$ particles-biofilm
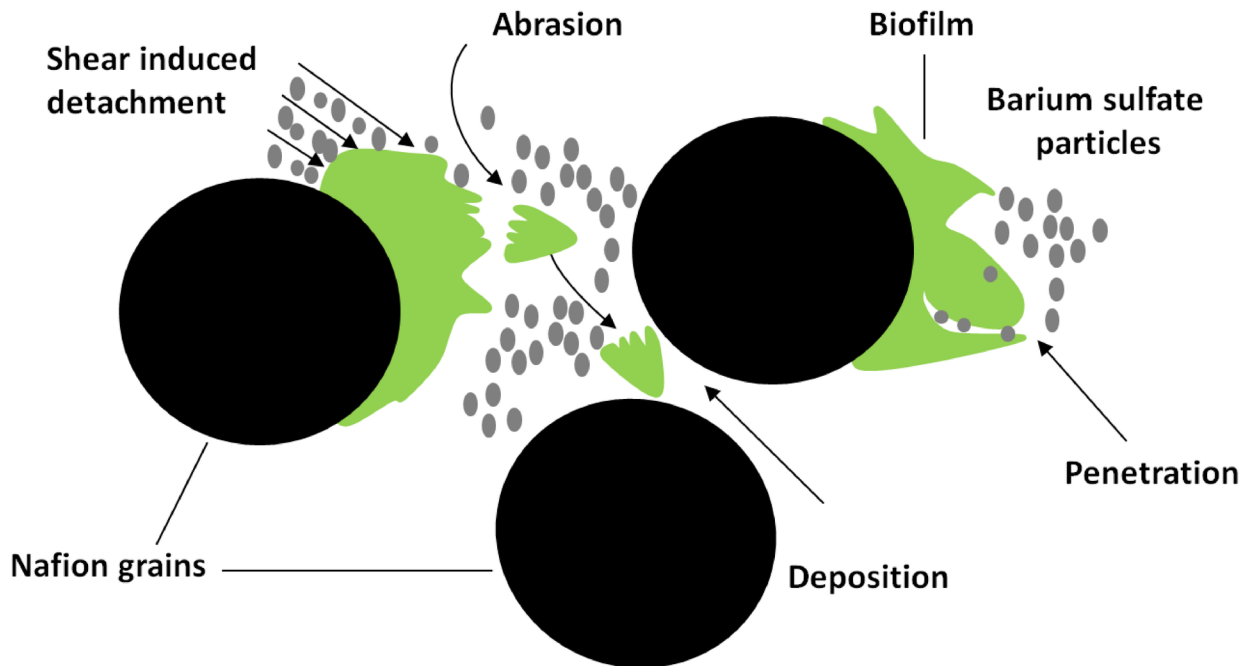
Fig 7. Schematic of biofilm detachment mechanisms during BaSO4 injection.

interactions also contributed to the detachment observed. Fig 7. illustrates the different mechanisms potentially causing the detachment. The shear and abrasion induced detachment explain the differences in the overall and local biofilm volumetric fractions observed. In Table 2, the low probability of the biofilm phase obtained with $BaSO_4$ to also belong to the biofilm phase obtained with $FeSO_4$ might also point to the deposition or filtration of some detached biofilm patches further upstream within the column.

Table 3 summarizes key points on which the method by [39] and the method presented here can be evaluated. The $FeSO_4$-based method allows to image biofilms in porous media using a non-toxic and non-destructive contrast agent on a X-ray lab source with movable detector. The combination of long STD and Lorentzian filter allows to substantially increase the signal to noise ratio. As mentioned earlier, the colloidal fraction observed for the control dataset (LControl) is not negligible. Nevertheless, the detected biofilm fraction in the LFeSO4 experiment is much higher which confirms that the higher volumetric fraction observed in the

Table 3. Evaluation of the presented method and another existing one for imaging biofilms in porous media.

	LFeSO4	*BaSO4*
Biofilm integrity	non-destructive	can cause detachment during *BaSO4* injection
Biofilm toxicity	none, but high inorganic content biofilm	none
Lab XCT requirements	movable detector	none
Imaging issues	High signal to noise ratio	Prone to beam hardening
Reconstruction requirements	Lorenztian filter	none
Segmentation	Thresholding	Combination of region growing and thresholding

latter case is due to biological activity, either due to the biofilm itself or to precipitation induced by bacterial activity, (e.g. iron oxidation, sulfide salts production, see [5] and [52]). The $BaSO_4$-based method provides clear contrast between the different phases but interactions of the $BaSO_4$ suspension with the biofilm induce substantial biofilm detachment. In both cases, some uncertainty remains related to the segmentation, which could however be quantified.

Conclusion

In this paper, we presented an innovative method to image biofilms in porous media combining iron sulfate as a contrast agent, a long STD and a Lorentzian filter. The non-toxic and non-destructive contrast agent was continuously added to the biofilm during the biofilm growth. The combination of using a large STD together with application of a Lorentzian Fourier filter allowed to exploit refraction effects. The reconstructed data showed a substantial reduction in noise and an increase in the contrast between materials exhibiting low attenuation coefficients differences, revealing the biofilm morphology. We found that in the porous medium and for the present growth conditions, the biofilm exhibits complex corrugated structures. We compared this method with an existing method using $BaSO_4$ as as a contrast agent for the exact same sample and observed some differences in the biofilm morphology obtained due to interactions between the biofilm and the $BaSO_4$. Namely, due to abrasion and shear detachment, more than 50% of the biofilm was washed out by the contrast agent emphasizing the need for non-destructive contrast agents for biofilm imaging in porous media. The method presented in this study delivers 3D biofilm morphologies in porous media non-destructively on a X-ray lab source. Possible applications are studies addressing the interplay between biofilms, their morphology and local hydrodynamic and mass transport processes in realistic porous media models.

Supporting information

S1 File. Segmentation of the $LFeSO_4$ data set.
(PDF)

S2 File. Segmentation of the $BaSO_4$ data set.
(PDF)

S3 File. Effect of the rheological properties of the $BaSO_4$ on the wall shear stress.
(PDF)

S4 File. Lorentzian Filer: Theoretical Background.
(PDF)

Acknowledgments

Author Contributions

Conceptualization: Maxence Carrel, Mario A. Beltran, Verónica L. Morales, Nicolas Derlon, Eberhard Morgenroth, Rolf Kaufmann, Markus Holzner.

Data curation: Maxence Carrel, Mario A. Beltran.

Formal analysis: Maxence Carrel, Mario A. Beltran.

Funding acquisition: Markus Holzner.

Investigation: Maxence Carrel, Mario A. Beltran.

Methodology: Maxence Carrel, Mario A. Beltran.

Project administration: Markus Holzner.

Resources: Maxence Carrel, Mario A. Beltran.

Software: Maxence Carrel, Mario A. Beltran.

Supervision: Maxence Carrel, Mario A. Beltran, Markus Holzner.

Validation: Maxence Carrel, Mario A. Beltran, Verónica L. Morales.

Writing – original draft: Maxence Carrel, Mario A. Beltran, Verónica L. Morales.

Writing – review & editing: Maxence Carrel, Mario A. Beltran, Verónica L. Morales, Nicolas Derlon, Eberhard Morgenroth, Markus Holzner.

References

1. Hall-Stoodley L, Costerton JW, Stoodley P. Bacterial biofilms: from the Natural environment to infectious diseases. Nature Reviews Microbiology. 2004; 2:95–108. https://doi.org/10.1038/nrmicro821 PMID: 15040259

2. Costerton J, Stewart PS, Greenberg EP. Bacterial Biofilms: A Common Cause of Persistent Infections. Science. 1999; 284:1318–1322. https://doi.org/10.1126/science.284.5418.1318 PMID: 10334980

3. Griebler C, Lueders T. Microbial biodiversity in groundwater ecosystems. Freshwater Biology. 2009; 54:649–677. https://doi.org/10.1111/j.1365-2427.2008.02013.x

4. Meckenstock RU, Elsner M, Griebler C, Lueders T, Stumpp C, Aamand J, et al. Biodegradation: Updating the Concepts of Control for Microbial Cleanup in Contaminated Aquifers. Environmental Science and Technology. 2015; 49:7073–7081. https://doi.org/10.1021/acs.est.5b00715 PMID: 26000605

5. Blowes DW, Ptacek CJ, Benner SG, McRae CWT, Bennett TA, Puls RW. Treatment of inorganic contaminants using permeable reactive barriers. Journal of Contaminant Hydrology. 2000; 45:123–137. https://doi.org/10.1016/S0169-7722(00)00122-4

6. Lappin-Scott HM, Cusack F, Costerton JW. Nutrient Resuscitation and Growth of Starved Cells in Sandstone Cores: a Novel Approach to Enhanced Oil Recovery. Applied and Environmental Microbiology. 1988; 54:1373–1382. PMID: 16347648

7. Ebigbo A, Helmig R, Cunningham AB, Class H, Gerlach R. Modelling biofilm growth in the presence of carbon dioxide and water flow in the subsurface. Advances in Water Resources. 2010; 33:762–781. https://doi.org/10.1016/j.advwatres.2010.04.004

8. Mitchell AC, Phillips A, Schultz L, Parks S, Spangler L, Cunningham AB, et al. Microbial CaCO3 mineral formation and stability in an experimentally simulated high pressure saline aquifer with supercritical CO2. International Journal of Greenhouse Gas Control. 2013; 15:86–96. https://doi.org/10.1016/j.ijggc.2013.02.001

9. Baveye P, Vandevivere P, Hoyle BL, DeLeo PC, de Lozada DS. Environmental Impact and Mechanisms of the Biological Clogging of Saturated Soils and Aquifer Materials. Critical Reviews in Environmental Science and Technology. 1998; 28:123–191. https://doi.org/10.1080/10643389891254197

10. Bouwer H. Artificial recharge of groundwater: hydrogeology and engineering. Hydrogeology Journal. 2002; 10(1):121–142. https://doi.org/10.1007/s10040-001-0182-4

11. Sand W. Microbial life in geothermal waters. Geothermics. 2003; 32:655–667. https://doi.org/10.1016/S0375-6505(03)00058-0

12. Seymour JD, Gage JP, Codd SL, Gerlach R. Anomalous Fluid Transport in Porous Media Induced by Biofilm Growth. Physical Review Letters. 2004; 93:198103. https://doi.org/10.1103/PhysRevLett.93. 198103 PMID: 15600886

13. Davit Y, Debenest G, Wood BD, Quintard M. Modeling non-equilibrium mass transport in biologically reactive porous media. Advances in Water Resources. 2010; 33:1075–1093. https://doi.org/10.1016/j. advwatres.2010.06.013

14. Golfier F, Wood BD, Orgogozo L, Quintard M, Buès M. Biofilms in porous media: Development of macroscopic transport equations via volume averaging with closure for local mass equilibrium conditions. Advances in Water Resources. 2009; 32:463–485. https://doi.org/10.1016/j.advwatres.2008.11.012

15. Kapellos GE, Alexiou TS, Payatakes AC. Theoretical modeling of fluid flow in cellular biological media: An overview. Mathematical Biosciences. 2010; 225:83–93. https://doi.org/10.1016/j.mbs.2010.03.003 PMID: 20303992

16. Orgogozo L, Golfier F, Buès M, Quintard M. Upscaling of transport processes in porous media with biofilms in non-equilibrium conditions. Advances in Water Resources. 2010; 33:585–600. https://doi.org/ 10.1016/j.advwatres.2010.03.004

17. Pintelon TRR, Graf von der Schulenburg DA, Johns ML. Towards optimum permeability reduction in porous media using biofilm growth simulations. Biotechnology and Bioengineering. 2009; 103:767–779. https://doi.org/10.1002/bit.22303 PMID: 19309753

18. von der Schulenburg DAG, Pintelon TRR, Picioreanu C, Van Loosdrecht MCM, Johns ML. Three-dimensional simulations of biofilm growth in porous media. AIChE Journal. 2009; 55:494–504. https:// doi.org/10.1002/aic.11674

19. Battin TJ, Sloan WT, Kjelleberg S, Daims H, Head IM, Curtis TP, et al. Microbial landscapes: new paths to biofilm research. Nature Reviews Microbiology. 2007; 5:76–81. https://doi.org/10.1038/nrmicro1556 PMID: 17170748

20. Milferstedt K, Pons MN, Morgenroth E. Analyzing characteristic length scales in biofilm structures. Biotechnology and Bioengineering. 2009; 102:368–379. https://doi.org/10.1002/bit.22075 PMID: 18949757

21. Stoodley P, Dodds I, De Beer D, Scott HL, Boyle JD. Flowing biofilms as a transport mechanism for biomass through porous media under laminar and turbulent conditions in a laboratory reactor system. Biofouling. 2005; 21:161–168. https://doi.org/10.1080/08927010500375524 PMID: 16371336

22. Rusconi R, Lecuyer S, Guglielmini L, Stone HA. Laminar flow around corners triggers the formation of biofilm streamers. Journal of The Royal Society Interface. 2010; 7:1293–1299. https://doi.org/10.1098/ rsif.2010.0096

23. Cunningham AB, Characklis WG, Abedeen F, Crawford D. Influence of biofilm accumulation on porous media hydrodynamics. Environmental Science and Technology. 1991; 25:1305–1311. https://doi.org/ 10.1021/es00019a013

24. Taylor S, Jaffé P. Biofilm growth and the related changes in the physical properties of a porous medium: 1. Experimental Investigation. Water Resources Research. 1990; 26:2153–2159. https://doi.org/10. 1029/WR026i009p02171

25. Dupin HJ, McCarty PL. Impact of Colony Morphologies and Disinfection on Biological Clogging in Porous Media. Environmental Science and Technology. 2000; 34:1513–1520. https://doi.org/10.1021/ es990452f

26. Kone T, Golfier F, Orgogozo L, Oltéan C, Lefévre E, Block JC, et al. Impact of biofilm-induced heterogeneities on solute transport in porous media. Water Resources Research. 2014; 50:9103–9119. https:// doi.org/10.1002/2013WR015213

27. Paulsen JE, Oppen E, Bakke R. Biofilm morphology in porous media, a study with microscopic and image techniques. Water Science and Technology. 1997; 36:1. https://doi.org/10.1016/S0273-1223 (97)00317-X

28. Sharp RR, Cunningham AB, Komlos J, Billmayer J. Observation of thick biofilm accumulation and structure in porous media and corresponding hydrodynamic and mass transfer effects. Water Science and Technology. 1999; 39:195. https://doi.org/10.1016/S0273-1223(99)00168-7

29. Thullner M, Zeyer J, Kinzelbach W. Influence of Microbial Growth on Hydraulic Properties of Pore Networks. Transport in Porous Media. 2002; 49:99–122. https://doi.org/10.1023/A:1016030112089

30. Vayenas DV, Michalopoulou E, Constantinides GN, Pavlou S, Payatakes AC. Visualization experiments of biodegradation in porous media and calculation of the biodegradation rate. Advances in Water Resources. 2002; 25:203–219. https://doi.org/10.1016/S0309-1708(01)00023-9

31. Derlon N, Peter-Varbanets M, Scheidegger A, Pronk W, Morgenroth E. Predation influences the structure of biofilm developed on ultrafiltration membranes. Water Research. 2012; 46:3323–3333. https:// doi.org/10.1016/j.watres.2012.03.031 PMID: 22534121

32. Wagner M, Taherzadeh D, Haisch C, Horn H. Investigation of the mesoscale structure and volumetric features of biofilms using optical coherence tomography. Biotechnology and Bioengineering. 2010; 107:844–853. https://doi.org/10.1002/bit.22864 PMID: 20717977

33. Xi C, Marks D, Schlachter S, Luo W, Boppart SA. High-resolution three-dimensional imaging of biofilm development using optical coherence tomography. Journal of Biomedical Optics. 2006; 11:034001–034006. https://doi.org/10.1117/1.2209962

34. Graf von der Schulenburg DA, Akpa BS, Gladden LF, Johns ML. Non-invasive mass transfer measurements in complex biofilm-coated structures. Biotechnology and Bioengineering. 2008; 101:602–608. https://doi.org/10.1002/bit.21913 PMID: 18727130

35. Wagner M, Manz B, Volke F, Neu TR, Horn H. Online assessment of biofilm development, sloughing and forced detachment in tube reactor by means of magnetic resonance microscopy. Biotechnology and Bioengineering. 2010; 107:172–181. https://doi.org/10.1002/bit.22784 PMID: 20506514

36. Vogt SJ, Sanderlin AB, Seymour JD, Codd SL. Permeability of a growing biofilm in a porous media fluid flow analyzed by magnetic resonance displacement-relaxation correlations. Biotechnology and Bioengineering. 2013; 110:1366–1375. https://doi.org/10.1002/bit.24803 PMID: 23239390

37. Wildenschild D, Vaz CMP, Rivers ML, Rikard D, Christensen BSB. Using X-ray computed tomography in hydrology: systems, resolutions, and limitations. Journal of Hydrology. 2002; 267:285–297. https://doi.org/10.1016/S0022-1694(02)00157-9

38. Wildenschild D, Sheppard AP. X-ray imaging and analysis techniques for quantifying pore-scale structure and processes in subsurface porous medium systems. Advances in Water Resources. 2013; 51:217–246. https://doi.org/10.1016/j.advwatres.2012.07.018

39. Davit Y, Iltis G, Debenest G, Veran-Tissoires S, Wildenschild D, Gerino M, et al. Imaging biofilm in porous media using X-ray computed microtomography. Journal of Microscopy. 2011; 242:15–25. https://doi.org/10.1111/j.1365-2818.2010.03432.x PMID: 21118226

40. Iltis GC, Armstrong RT, Jansik DP, Wood BD, Wildenschild D. Imaging biofilm architecture within porous media using synchrotron-based X-ray computed microtomography. Water Resources Research. 2011; 47:W02601. https://doi.org/10.1029/2010WR009410

41. Rolland du Roscoat S, Martins JMF, Séchet P, Vince E, Latil P, Geindreau C. Application of synchrotron X-ray microtomography for visualizing bacterial biofilms 3D microstructure in porous media. Biotechnology and Bioengineering. 2014; 111:1265–1271. https://doi.org/10.1002/bit.25168 PMID: 24293082

42. Ivankovic T, Rolland du Roscoat S, Geindreau C, Séchet P, Huang Z, Martins JMF. Development and evaluation of an experimental protocol for 3-D visualization and characterization of the structure of bacterial biofilms in porous media using laboratory X-ray tomography. Biofouling. 2016; 32:1235–1244. https://doi.org/10.1080/08927014.2016.1249865 PMID: 27827532

43. Peszynska M, Trykozko A, Iltis G, Schlueter S, Wildenschild D. Biofilm growth in porous media: Experiments, computational modeling at the porescale, and upscaling. Advances in Water Resources. 2015; 95:288–301 https://doi.org/10.1016/j.advwatres.2015.07.008

44. Stoodley P, deBeer D, Lewandowski Z. Liquid Flow in Biofilm Systems. Applied and Environmental Microbiology. 1994; 60:2711–2716. PMID: 16349345

45. Blauert F, Horn H, Wagner M. Time-resolved biofilm deformation measurements using optical coherence tomography. Biotechnology and Bioengineering. 2015; 112:1893–1905. https://doi.org/10.1002/bit.25590 PMID: 25786671

46. Möhle RB, Langemann T, Haesner M, Augustin W, Scholl S, Neu TR, et al. Structure and shear strength of microbial biofilms as determined with confocal laser scanning microscopy and fluid dynamic gauging using a novel rotating disc biofilm reactor. Biotechnology and Bioengineering. 2007; 98:747–755. https://doi.org/10.1002/bit.21448 PMID: 17421046

47. Li L, Benson CH, Lawson EM. Impact of Mineral Fouling on Hydraulic Behavior of Permeable Reactive Barriers. Groundwater. 2005; 43:582–596. https://doi.org/10.1111/j.1745-6584.2005.0042.x

48. Anderson RT, Vrionis HA, Ortiz-Bernad I, Resch CT, Long PE, Dayvault R, et al. Stimulating the In Situ Activity of Geobacter Species To Remove Uranium from the Groundwater of a Uranium-Contaminated Aquifer. Applied and Environmental Microbiology. 2003; 69:5884–5891. PMID: 14532040

49. Omoregie EO, Couture RM, Van Cappellen P, Corkhill CL, Charnock JM, Polya DA, et al. Arsenic Bioremediation by Biogenic Iron Oxides and Sulfides. Applied and Environmental Microbiology. 2013; 79:4325–4335. PMID: 23666325

50. Benner SG, Blowes DW, Ptacek CJ, Mayer KU. Rates of sulfate reduction and metal sulfide precipitation in a permeable reactive barrier. Applied Geochemistry. 2002; 17:301–320. https://doi.org/10.1016/S0883-2927(01)00084-1

51. Teixeira S, Vieira MN, Marques JE, Pereira R. Bioremediation of an Iron-Rich Mine Effluent by Lemna minor. International Journal of Phytoremediation. 2014; 16:1228–1240. https://doi.org/10.1080/15226514.2013.821454 PMID: 24933914

52. Weiner ER. In: Applications of Environmental Aquatic Chemistry. CRC Press; 2013. p. 592.

53. Paganin D. In: Coherent x-ray optics. Oxford University Press; 2006. p. 411.

54. Wilkins SW, E GT, Gao D, Pogany A, Stevenson AW. Phase-contrast imaging using polychromatic hard X-rays. Nature. 1996; 384:335–338. https://doi.org/10.1038/384335a0

55. Beltran MA, Paganin DM, Uesugi K, Kitchen MJ. 2D and 3D X-ray phase retrieval of multi-material objects using a single defocus distance. Optics Express. 2010; 18:6423–6436. https://doi.org/10.1364/OE.18.006423 PMID: 20389666

56. Beltran MA, Paganin DM, Siu KKW, Fouras A, Hooper SB, Reser DH, Kitchen MJ. Interface-specific x-ray phase retrieval tomography of complex biological organs. Physics in Medicine and Biology. 2011; 56:7353–7369. https://doi.org/10.1088/0031-9155/56/23/002 PMID: 22048612

57. Downie H, Holden N, Otten W, Spiers AJ, Valentine TA, Dupuy LX. Transparent Soil for Imaging the Rhizosphere. PLoS ONE. 2012; 7:e44276. https://doi.org/10.1371/journal.pone.0044276 PMID: 22984484

58. Holzner M, Morales VL, Willmann M, Dentz M. Intermittent Lagrangian velocities and accelerations in three-dimensional porous medium flow. Physical Review E. 2015; 92:013015. https://doi.org/10.1103/PhysRevE.92.013015

59. Plouraboué F, Cloetens P, Fonta C, Steyer A, Lauwers F, Marc-Vergnes JP. X-ray high-resolution vascular network imaging. Journal of Microscopy. 2004; 215:139–148. https://doi.org/10.1111/j.0022-2720.2004.01362.x PMID: 15315500

60. Feldkamp LA, Davis LC, Kress JW. Practical cone-beam algorithm. Journal of the Optical Society of America A. 1984; 1:612–619. https://doi.org/10.1364/JOSAA.1.000612

61. Paganin D, Mayo SC, Gureyev TE, Miller PR, Wilkins SW. Simultaneous phase and amplitude extraction from a single defocused image of a homogeneous object. Journal of Microscopy. 2002; 206:33–40. https://doi.org/10.1046/j.1365-2818.2002.01010.x PMID: 12000561

62. Arhatari BD, Gates WP, Eshtiaghi N, Peele AG. Phase retrieval tomography in the presence of noise. Journal of Applied Physics. 2010; 107:034904. https://doi.org/10.1063/1.3298930

63. Burvall A, Lundström U, Takman PAC, Larsson DH, and Hertz, Hans M. Phase retrieval in X-ray phase-contrast imaging suitable for tomography. Optics Express. 2011; 19:10359–10376. https://doi.org/10.1364/OE.19.010359 PMID: 21643293

64. Gureyev TE, Paganin DM, Myers GR, Nesterets YI, Wilkins SW. Phase-and-amplitude computer tomography. Applied Physics Letters. 2006; 89:034102. https://doi.org/10.1063/1.2226794

65. Mayo SC, Davis TJ, Gureyev TE, Miller PR, Paganin D, Pogany A, et al. X-ray phase-contrast microscopy and microtomography. Optics Express. 2003; 11:2289–2302. https://doi.org/10.1364/OE.11.002289 PMID: 19471337

66. Myers GR, Gureyev TE, Paganin DM, Mayo SC. The binary dissector: phase contrast tomography of two- and three-material objects from few projections. Optics Express. 2008; 16:10736–10749. https://doi.org/10.1364/OE.16.000908 PMID: 18607490

67. Carrel M. Digital Rocks data repository. http://www.dx.doi.org/10.17612/P7Q07W

68. Leemann A, Loser R, Münch B. Influence of cement type on ITZ porosity and chloride resistance of self-compacting concrete. Cement and Concrete Composites. 2010; 32:116–120. https://doi.org/10.1016/j.cemconcomp.2009.11.007

69. Münch B. Empa Bundle of ImageJ Plugins for Image Analysis (EBIPIA). http://wiki.imagej.net/Xlib

70. Adams R, Bischof L. Seeded region growing. IEEE Transactions on Pattern Analysis and Machine Intelligence. 1994; 16:641–647. https://doi.org/10.1109/34.295913

71. Derlon N, Massé A, Escudié R, Bernet N, Paul E. Stratification in the cohesion of biofilms grown under various environmental conditions. Water Research. 2008; 42:2102–2110. https://doi.org/10.1016/j.watres.2007.11.016 PMID: 18086485

72. Rochex A, Massé A, Escudié R, Godon JJ, Bernet N. Influence of abrasion on biofilm detachment: evidence for stratification of the biofilm. Journal of Industrial Microbiology & Biotechnology. 2009; 36:467–470. https://doi.org/10.1007/s10295-009-0543-x

73. Stoodley P, Cargo R, Rupp JC, Wilson S, Klapper I. Biofilm material properties as related to shear-induced deformation and detachment phenomena. Journal of Industrial Microbiology and Biotechnology. 2002; 29:361–367. https://doi.org/10.1038/sj.jim.7000282 PMID: 12483479